(Received 28 October 2025, Accepted 8 May 2026, Scheduled 5 June 2026)

Design and Analysis of a Novel Switched Reluctance Motor Utilizing Embedded Permanent Magnets for Torque Enhancement

Matin Rahimi, Seyed H. Shahalami*, and Esmaeil F. Choolabi

Department of Electrical Engineering, University of Guilan, Rasht, Iran

ABSTRACT: This research presents a high-performance 24/22 hybrid-excited switched reluctance motor (HESRM) featuring a modular C-core, dual-tooth topology engineered for superior torque density and efficiency. The proposed architecture utilizes a strategic flux-concentration mechanism by embedding permanent magnets (PMs) exclusively within the inter-tooth spaces. This targeted integration establishes a dual-path flux enhancement that intensifies air-gap flux density while suppressing stator yoke saturation. To ensure methodological rigor, structural parameters were optimized using a Multi-Objective Genetic Algorithm (GA) to maximize average torque. Additionally, a Magnetic Equivalent Circuit (MEC) model was derived to analytically interpret the PM-assisted torque enhancement. The design is rigorously validated through Three-Dimensional Finite Element Analysis (3D FEA), accounting for end-leakage effects. The 3D FEA results yield an average torque of 3 N · m, exhibiting excellent agreement with the 2D FEA estimation (2.98 N · m). Detailed evaluations of losses and efficiency mapping reveal that the HSSRM 24/22 achieves a 43% increase in average torque and significantly higher efficiency than the reference HSRM 12/10. Ultimately, this study offers a robust, cost-effective solution with an enhanced torque-per-PM-volume ratio for advanced electric drive applications.

1. INTRODUCTION

Switched reluctance motors (SRMs) are popular due to their simple structure and low manufacturing cost; however, their low power density imposes limitations on industrial applications. To improve torque performance, segmented topologies and the integration of permanent magnets (PMs) have been proposed. Recent literature can be categorized into four major technical trends: A. Segmented and Modular Stator/Rotor Topologies. The use of segmented structures has been proven effective in reducing magnetic path lengths and improving fault tolerance. Studies in [1–3] have investigated segmented rotor designs to enhance power density in aircraft and critical applications, where the rotor segments allow for independent flux paths. Similarly, modular stator configurations, such as C-core [4, 5] and E-core [6] structures, have been proposed to simplify winding manufacturing and isolate phase flux. Furthermore, axial-flux segmented-stator designs [7] and dual-modular AFM-HSRM [8] have been investigated to maximize the active surface area and torque density. Despite these advancements, many segmented designs face challenges in mechanical robustness and localized magnetic saturation at the segment interfaces, which limit their high-speed capability. B. Hybrid-Excited and PM-Assisted SRMs Integrating PMs into the SRM structure is a dominant trend for boosting torque density and improving flux control. Hybrid reluctance motors (HRMs) using ferrite magnets [9, 10] or internal PMs [2, 11] have demonstrated significant efficiency gains compared to conventional SRMs. Strategic PM placement on the stator yoke [12], within stator tooth slots [13], or between poles [14, 15] has been shown to improve performance and reliability [16–19]. Innovative designs like the π-type modular stator [20] and hybrid-excited multi-phase configurations [21, 22] utilize circumferentially magnetized PMs to augment output torque and reduce magnetic saturation. However, the effective management of auxiliary PM flux to prevent irreversible demagnetization while maintaining a compact size remains a critical research gap. C. Multi-tooth and Structural Variations Structural modifications at the tooth level significantly influence electromagnetic performance. Multi-tooth stator designs [23–25] have been proposed to extend the speed range and increase torque output by increasing the number of strokes per revolution. Comparative studies in [26] highlight that unequal-tooth designs can drastically affect torque ripple and average torque. Modular 12/8 and HSRM 12/10 topologies with dual-tooth segments [27–30] have shown great promise for electric vehicle (EV) drives. While multi-tooth structures increase the torque-producing zones, they often lead to increased magnetic congestion in the stator teeth and complicated flux linkages that are difficult to optimize manually. D. Advanced Flux Management and Efficiency Optimization. To further push the boundaries of energy conversion, hybrid-excited multi-tooth motors [31] and designs with PMs embedded between stator teeth [22] have been analyzed for their ability to enhance air-gap flux and improve electromagnetic torque. Comparative analyses among various PM-assisted machines (HETSPM, TBFPM, and TBFSPM) in [21] offer insights into the trade-offs between

* Corresponding author: Seyed Hamid Shahalami (shahalami@guilan.ac.ir).

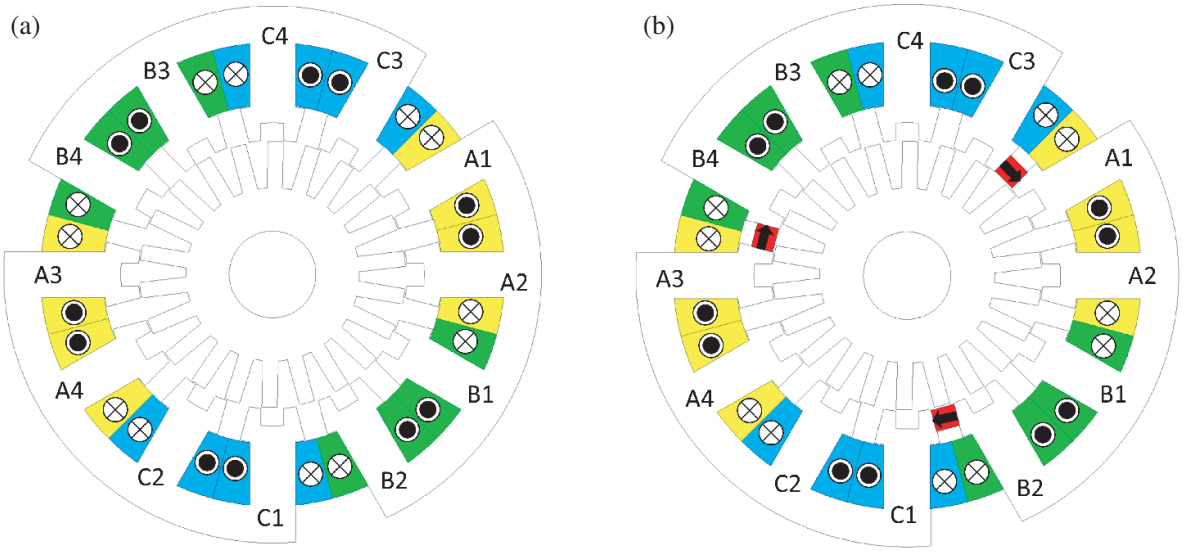

FIGURE 1. The topology of a 24/22 switched reluctance motor is shown in part (a), and part (b) depicts the topological structure of the 24/22 hybrid switched reluctance motor.

average torque and efficiency. Nevertheless, the synergy between a high pole count configuration (such as 24/22) and a dual-tooth modular stator has not been fully explored, particularly regarding the simultaneous improvement of torque density and efficiency using advanced materials.

The primary technical contributions of this research, which distinguish the proposed architecture from existing modular and hybrid-excited designs, are categorized into four fundamental pillars: (I) Structural Synthesis: The introduction of a novel 24/22 modular dual-tooth C-core stator topology that optimizes the magnetic path length and enhances the winding utilization factor; (II) Flux Engineering Strategy: A strategic PM placement exclusively within the inter-tooth gaps to facilitate a dual-path flux concentration mechanism, thereby intensifying air-gap flux density and mitigating stator yoke saturation; (III) Analytical and Methodological Rigor: The implementation of a Multi-Objective Genetic Algorithm (GA) for systematic structural optimization (detailed in Section 2) and the derivation of a Magnetic Equivalent Circuit (MEC) model to provide a theoretical interpretation of the PM-assisted torque enhancement; and (IV) Multi-Dimensional Validation: A rigorous verification process using Three-Dimensional Finite Element Analysis (3D FEA) to account for end-leakage and fringing effects. The 3D FEA results confirm an average torque of 3 N · m, exhibiting a high degree of correlation with the 2D FEA estimation of 2.98 N · m. Furthermore, the inclusion of a detailed iron/copper loss model and efficiency mapping provides a comprehensive performance benchmark. The remainder of this paper is organized as follows. Section 2 describes the HSSRM 24/22 structure, MEC modeling, and GA-based optimization framework. Section 3 presents the FEA-based static and dynamic analysis (including 3D FEA validation) and technical comparisons with the reference HSRM 12/10. Finally, Section 4 concludes the findings.

2. PROPOSED MOTOR STRUCTURE

2.1. Structure

Figure 1(a) illustrates the structure of a three-phase 24/22 switched reluctance motor. This motor features a stator with 24 teeth and a rotor with 22 teeth. The stator is composed of three separate C-shaped segments, each equipped with concentrated windings. Each segment includes four poles and two teeth; therefore, the stator has a total of twelve poles and 24 teeth. The rotor contains no permanent magnetic sources and consists solely of 22 teeth.

The two-tooth hybrid switched reluctance motor (as shown in Figure 1(b)) has a structure very similar to that of the proposed switched reluctance motor, with the key difference being the inclusion of three permanent magnets to enhance magnetic flux. These magnets are placed consecutively and innovatively between the end teeth of adjacent modules, sharing the same polarity. Importantly, these magnets do not occupy the space allocated for the windings.

2.2. Principle of Operation

The operation of the proposed motor is schematically illustrated in Figure 2. In Figure 2(a), the structure without permanent magnets is shown, where one of the phase windings is energized. In Figure 2(b), when the windings are not energized, the magnetic flux produced by the permanent magnets circulates within the stator segments and does not enter the air gap. In Figure 2(c), the permanent magnets play a key role in enhancing the magnetic flux; when one of the phase windings is energized, the flux generated by the magnets combines with the flux from the winding, resulting in an increased total flux passing through the air gap. This directly leads to an increase in the motor torque.

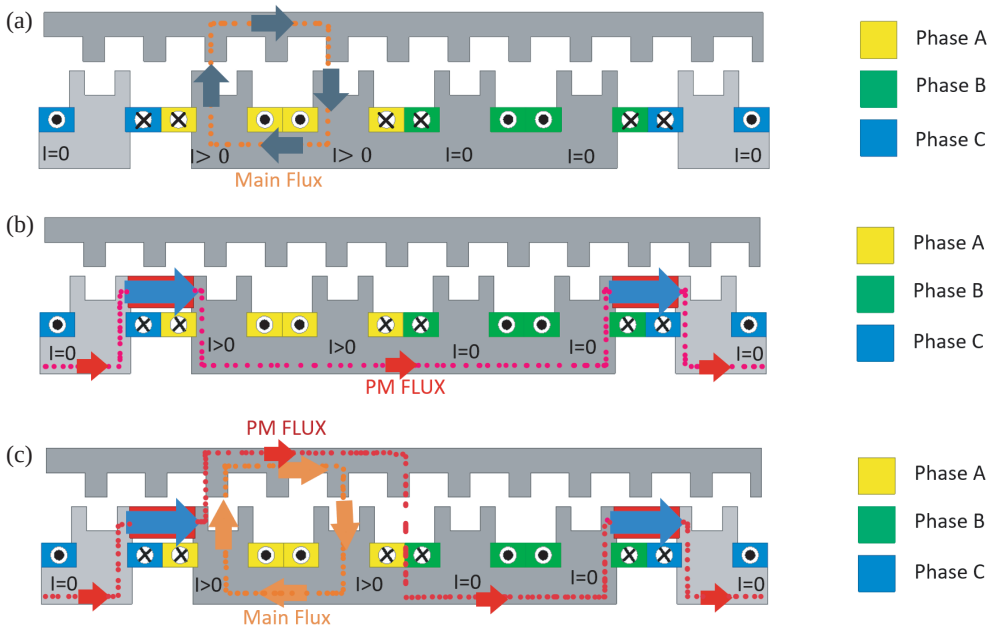

FIGURE 2. The motor operation is shown in three different conditions. (a) The magnetic flux path in the hybrid switched reluctance motor is illustrated when only the electrical current is applied, and the permanent magnets are inactive, (b) the magnetic flux generated by the permanent magnets is shown when no current flows through the windings, (c) the magnetic flux path is depicted when both the electrical current is applied and the permanent magnets are active.

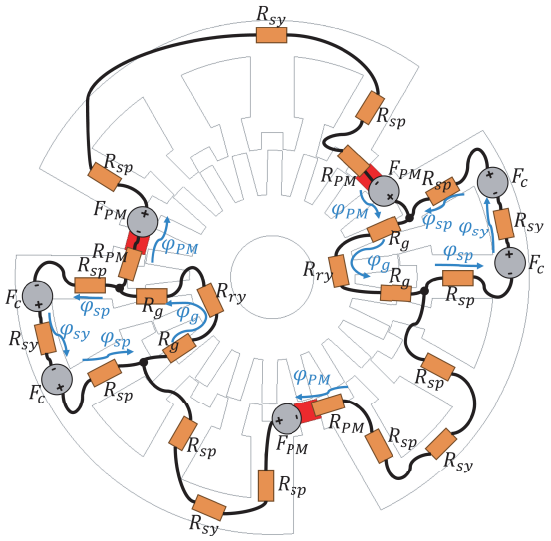

FIGURE 3. Equivalent magnetic circuit model (MCM) of the proposed 24/22 HSSRM.

2.3. Analytical Characterization of Operating Principles Utilizing the Magnetic Equivalent Circuit Framework

To evaluate the fundamental operation of the Permanent Magnet Switched Reluctance Motor, the Magnetic Equivalent Circuit (MEC) is derived, as illustrated in Figure 3 for the energized state of Phase A. In this simplified analytical framework, R_{sp}, R_{sy}, R_{ry}, R_g, and R_{pm} represent the magnetic reluctances of the stator pole, stator yoke, rotor yoke, air gap, and permanent magnet, respectively. Furthermore, F_c and F_{pm} denote the Magnetomotive Forces (MMFs) generated by the excited coil and the permanent magnets. The corresponding magnetic fluxes through the permanent magnets, stator pole, stator yoke, and air gap are designated as φ_{pm}, φ_{sp}, φ_{sy}, and φ_g. By leveraging Kirchhoff's Voltage and Current Laws (KVL and KCL) within the magnetic domain, the governing equations of the MEC are formulated as (1) and (2).

$$\begin{cases} 2R_{sp} + (2R_g + R_{ry})\,\varphi_g + R_{sy}\varphi_{sy} = 2F_c \\ (3R_{sy}+3R_{pm}+6R_{sp})\,\varphi_{pm}+(4R_g + 2R_{ry})\varphi_g = 3F_{pm} \end{cases} \tag{1}$$

$$\begin{cases} \varphi_{sy} = \varphi_{sp} \\ \varphi_{pm} = \varphi_g - \varphi_{sp} \end{cases} \tag{2}$$

Substituting (1) into (2) and simplifying yields the following expression:

$$\phi = R^{-1}F \tag{3}$$

where the MMF and flux matrices, denoted by F and ϕ, are defined as shown in (4) and (5), respectively.

$$\phi = [\varphi_{sp} \quad \varphi_g]^T \tag{4}$$

$$F = [2F_c \quad 3F_{pm}]^T \tag{5}$$

The reluctance matrix R comprises the following elements:

$$\begin{cases} R_{11} = 2R_{sp} + R_{sy} \\ R_{12} = 2R_g + R_{ry} \\ R_{21} = -3R_{sy} - 3R_{pm} - 6R_{sp} \\ R_{22} = 3R_{sy} + 3R_{pm} + 6R_{sp} + 4R_g + 2R_{ry} \end{cases} \tag{6}$$

To evaluate (3), it is necessary to determine the determinant of the reluctance matrix, det R, as formulated in (7).

$$\begin{aligned} \det R = {} & (2R_{sp}+R_{sy})\,(3R_{sy}+3R_{pm}+6R_{sp}+4R_g+2R_{ry}) \\ & +(3R_{sy} + 3R_{pm} + 6R_{sp})(2R_g + R_{ry}) \end{aligned} \tag{7}$$

Given that $3R_{pm} \gg 3R_{sy}+6R_{sp}+4R_g+2R_{ry}$ and $3R_{pm} \gg 3R_{sy}+6R_{sp}$, (7) can be simplified to the following approximation:

$$\det R \approx 3R_{pm}(2R_{sp}+R_{sy}+2R_g+R_{ry}) \tag{8}$$

The resulting equations are thus yielded as:

$$\varphi_{sp} = \frac{3R_{sy}+3R_{pm}+6R_{sp}+4R_g+2R_{ry}}{3R_{pm}(2R_{sp}+R_{sy}+2R_g+R_{ry})}$$

$$\cdot 2F_c - \frac{2R_g+R_{ry}}{3R_{pm}(2R_{sp}+R_{sy}+2R_g+R_{ry})} \cdot 3F_{pm} \tag{9}$$

$$\varphi_g = \frac{3R_{sy}+3R_{pm}+6R_{sp}}{3R_{pm}(2R_{sp}+R_{sy}+2R_g+R_{ry})}$$

$$\cdot 2F_c + \frac{2R_{sp}+R_{sy}}{3R_{pm}(2R_{sp}+R_{sy}+2R_g+R_{ry})} \cdot 3F_{pm} \tag{10}$$

The electromagnetic torque production in the proposed HSSRM 24/22 is rigorously derived using the magnetic co-energy method, integrated with a Magnetic Circuit Model (MCM). Unlike conventional methods that rely solely on simplified look-up tables, the torque here is extracted by analyzing the state-space energy conversion within the modular C-core segments.

To calculate the torque, the magnetic co-energy (W') must first be determined. For a given phase current (i) and rotor position (θ), the co-energy represents the area under the flux linkage-current ($\psi - i$) characteristic, defined as:

$$W'(\theta, i) = \int_0^i \psi(\theta, i) di \tag{11}$$

The instantaneous electromagnetic torque (T) is then obtained by taking the partial derivative of the magnetic co-energy with respect to the rotor angular position at a constant excitation current:

$$T(\theta, i) = \frac{\partial W'(\theta, i)}{\partial \theta} |i = \text{const} \tag{12}$$

To enhance the accuracy of this extraction, a detailed Magnetic Circuit Model (MCM) is employed to characterize the flux linkage $\psi(\theta, i)$. The MCM accounts for the nonlinear permeance of the M19-29G steel and the auxiliary MMF provided by the SH-class permanent magnets. By considering the air-gap reluctance (R_g) as a function of θ and the saturation of the modular stator teeth, the total flux linkage is expressed as:

$$\psi(\theta, i) = N\varphi(\theta, i) \tag{13}$$

where N is the number of turns per phase. By substituting this relationship into the co-energy integral, the torque production mechanism is precisely modeled, capturing the enhancement effects of the hybrid excitation on the total output torque.

2.4. Physical Justification and Magnetic Flux Interaction Analysis

To provide a deeper understanding of the torque enhancement in the proposed HSSRM 24/22, the magnetic flux interaction within the modular structure is analyzed. Figure 2 illustrates the simplified linear representation of the magnetic circuit, highlighting the paths for the permanent magnet flux (PM Flux) and the excitation flux (Main Flux).

The technical advantages of this structure over the designs in [14, 28, 31] are summarized as follows:

- Flux Reinforcement Mechanism: As shown in Figure 2, the PMs are positioned between the C-core modules. When a phase is energized ($I > 0$), the MMF produced by the concentrated windings generates a main flux that follows a short path through the modular segment. The PM flux is directed in the same orientation, creating a constructive superposition. This results in a significantly higher flux improvement factor ($\Delta\psi$) at the tooth-pole interface.

- Reduced Magnetic Reluctance: The dual-tooth C-core modular stator eliminates the need for a long magnetic return path through a conventional back-iron (yoke). This structural modification reduces the total magnetic reluctance (R_m), allowing for higher magnetic loading.

- Flux Concentration Effect: The PMs act as magnetic barriers that prevent the excitation flux from leaking into adjacent inactive segments. This focusing effect ensures that the maximum possible flux is linked with the rotor poles during the high-torque production zone, leading to a maximized $\frac{d\psi}{d\theta}$.

This physical synergy, demonstrated by the FEA flux density plots in Figure 8, confirms that the HSSRM 24/22 achieves a superior torque-to-volume ratio by optimizing the magnetic circuit paths, providing a robust theoretical justification for its improved performance compared to the reference 12/10 topologies.

2.5. Design Aspects and Optimization of Key Parameters

To enhance torque performance in switched reluctance motors, researchers in studies [4, 14, 15 17, 31] have utilized multi-tooth structures. The results of these investigations indicate that a two-tooth topology provides better torque generation, a finding that is also confirmed in studies [4, 14].

To calculate the electromagnetic torque in a switched reluctance motor with m teeth per stator pole, the method presented in [14] can be employed.

$$T_e = \int_0^I \frac{N^2 I \mu_0 m l_r}{2 l_g} dI = \frac{N^2 I^2 \mu_0 m l_r}{4 l_g} \tag{14}$$

In this expression, l_g and l denote the air-gap length and stack length, respectively; N is the number of turns per phase, and μ_0 is the permeability of free space. Therefore, the proposed design, by increasing m, enhances the output torque. As evident

from this formula, increasing the number of teeth (m) results in higher output torque.

The use of permanent magnet materials with controlled magnetic flux presents an innovative approach to improving motor performance. These materials reduce magnetic saturation in the stator poles and decrease magnetic reluctance, ultimately increasing the magnetic flux in the air gap and significantly enhancing the motor torque.

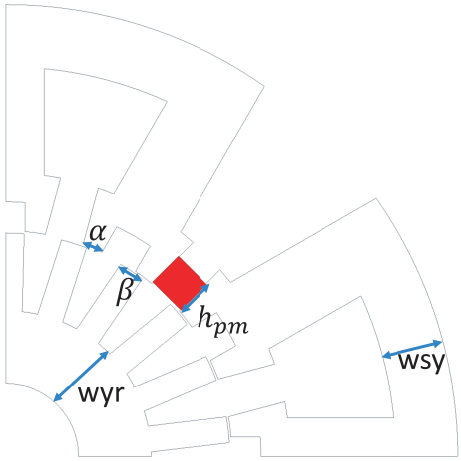

FIGURE 4. Key parameters of the proposed motors.

In this study, three key motor characteristics are optimized through a parametric analysis based on the finite element method to evaluate their impact on torque generation. As shown in Figure 4, these features include:

- Stator pole tooth angle (α)
- Rotor pole angle (β)
- Thickness of the permanent magnet between stator pole teeth (h_{pm})

In Figure 5(a), the variation of torque due to changes in the stator and rotor tooth arcs is presented. To investigate these variations, finite element analysis (FEA) was performed for a total of 81 different cases. In these analyses, the stator tooth arc was varied from 4° to 6° with a step of 0.25°, while the rotor tooth arc was examined over the same range and step size. It should be noted that the torque values were obtained through static magnetic simulations under a current of 12 A, at the position where the motor transitions from the aligned to the unaligned state corresponding to the maximum torque. Based on the results, the optimal tooth arcs for the stator and rotor were determined to be 5.13° and 6°, respectively.

In Figure 5(b), the effect of permanent magnet thickness on torque is evaluated, with the stator and rotor tooth arcs set to their optimal values. In this analysis, the magnets are embedded only between the stator teeth, and their thickness is varied from 1 mm to 7 mm in steps of 0.25 mm to assess its influence on torque. The results indicate that a magnet thickness of 5 mm between the stator teeth is the most suitable value.

2.6. Advanced Structural Refinement via Multi-Objective Genetic Algorithm (GA)

To ensure that the proposed HSSRM 24/22 achieves its peak performance and to overcome the inherent limitations of manual parametric scanning (which may neglect complex nonlinear couplings between design variables), a systematic optimization framework based on the Multi-Objective Genetic Algorithm (GA) was developed. This optimization was performed within the ANSYS Maxwell environment, utilizing 2D Transient Finite Element Analysis (FEA) coupled with a Current-Chopping Control (CCC) strategy to ensure that the dynamic effects of switching and magnetic saturation were accurately captured.

The optimization problem is formally structured to maximize the average output torque, defined by the following objective function:

$$Maximize\ f(x) = T_{avg}(\alpha, \beta, h_{pm}) \tag{15}$$

where the design vector x comprises the following critical geometric parameters:

- Stator Pole Tooth Arc (α): This parameter regulates the flux density distribution within the modular C-core and the available slot area for concentrated windings.
- Rotor Pole Arc (β): This variable determines the effective overlap area between the stator and rotor teeth, which is the primary zone of torque production.
- Permanent Magnet Thickness (h_{pm}): This dimension governs the amount of auxiliary flux injected into the magnetic circuit and the saturation levels of the stator poles.

The GA parameters were set with a population size of 30 and a termination criterion of 5 generations. The procedural flowchart of this heuristic search is depicted in Figure 6(a), illustrating the steps from initial population generation to the extraction of the optimal set. The convergence characteristic of the fitness function (average torque) across 180 distinct evaluations is presented in Figure 6(b). It is observed that the algorithm exhibits robust convergence toward the global maximum, effectively navigating the multi-dimensional design space.

The efficacy of the GA-based optimization is quantitatively validated in Table 1, which compares the final optimized dimensions with those obtained through the initial manual scan. The GA refined the stator and rotor pole arcs to 5.18° and 6.67°, respectively. Furthermore, the PM thickness was optimized to

TABLE 1. Comparison of design parameters and torque performance between the initial manual search and the proposed GA optimization framework.

Design Parameter	Initial Manual Method	Proposed GA Method
Stator tooth arc (°)	5.13	5.18
Rotor tooth arc (°)	6	6.67
PM Thickness (mm)	5	4.99
Max. Average Torque (N · m)	2.9626	3.4634

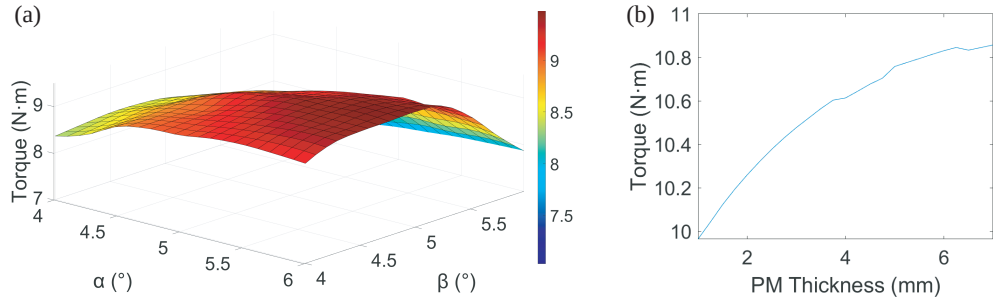

FIGURE 5. (a) Torque variation with changes in the stator and rotor pole tooth arcs. (b) Effect of varying the thickness of the permanent magnets placed between the stator pole teeth on torque.

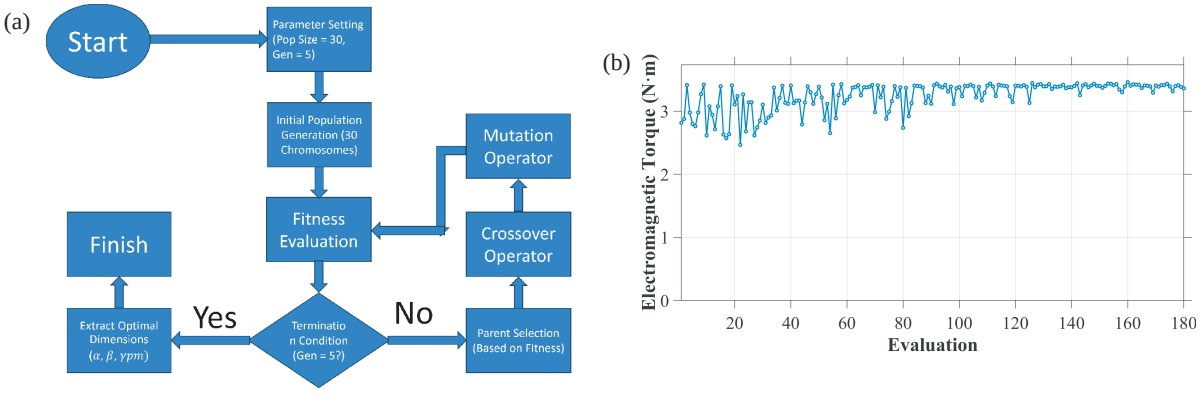

FIGURE 6. Optimization process of the proposed HSSRM: (a) procedural flowchart of the implemented multi-objective genetic algorithm (GA), and (b) convergence characteristic of the average electromagnetic torque across 180 fitness evaluations.

4.99 mm, representing a reduction compared to the initial design of 5 mm. This optimization process ultimately yielded a maximized average torque of 3.46 N · m, confirming a superior torque-per-PM-volume ratio and providing a scientifically sound justification for the final structural configuration of the HSSRM 24/22.

The characteristics and dimensions of the design parameters for the proposed motors are summarized in Table 2.

3. EVALUATION OF THE SIMULATION RESULTS FOR THE TWO PROPOSED MOTORS AND COMPARISON OF THEIR PERFORMANCE WITH EACH OTHER AND WITH OTHER REFERENCE MOTORS

3.1. Flux Paths and Distribution of Magnetic Flux Density

Figure 7 illustrates the flux line patterns of the newly designed Switched Reluctance Motor in both aligned and unaligned positions. In this design, the flux paths are shorter, leading to a significant reduction in iron core losses. Furthermore, due to the motor's unique structure, the occurrence of flux reversal or directional change within the iron core is minimal. This feature prevents the generation of negative torque and contributes to maintaining high motor efficiency.

The magnetic flux density distributions of the conventional SRM and the proposed HSSRM are comparatively analyzed in Figure 8. For the conventional SRM (Figures 8(a)–(b)), at a 12 A excitation, the flux density reaches 1.8 T in the yoke and 2 T in the teeth in the aligned position. This indicates a high degree of saturation throughout the magnetic circuit, which contributes to increased hysteresis losses.

In contrast, the proposed Hybrid HSSRM (Figures 8(c)–(d)) demonstrates a more optimized flux distribution. In the aligned position at 12 A, while the flux density in the teeth remains at 2 T to ensure high torque density, the value in the stator yoke is significantly reduced to 1.4 T.

Causal Analysis: This phenomenon is attributed to the strategic placement of SH-class magnets between the modular teeth. These magnets provide an auxiliary MMF that aligns with the excitation flux, effectively pushing the magnetic field toward the rotor poles. Consequently, the magnetic load on the stator yoke is alleviated, preventing deep saturation in the back iron while maximizing the flux concentration in the active torque-producing zones (the teeth). This structural synergy explains the 5.82% efficiency gain, as it minimizes the volume of steel operating under high-frequency saturation.

3.2. Flux Linkage and Inductance Diagrams

Figure 9 illustrates the relationships between flux linkage and inductance for the Switched Reluctance and hybrid Switched Reluctance Motors under different excitation currents.

- Figure 9(a) shows the flux linkage of the Switched Reluctance Motor versus rotor position, where 0° and 180° correspond to the unaligned and aligned positions, respec-

TABLE 2. Main dimensions and parameters of the proposed and compared motors.

Parameters	SSRM 24/22 (Proposed)	HSSRM 24/22 (Proposed)	SRM 12/10	HSRM 12/10
Number of phases	3	3	3	3
Number of stator and rotor poles	24/22	24/22	12/10	12/10
Stator outer diameter (mm)	124	124	124	124
Stator inner diameter (mm)	62	62	62	62
Stator yoke width (mm)	8.5	8.5	8.5	8.5
Rotor yoke width (mm)	10	10	10	10
Shaft diameter (mm)	20	20	20	20
Active axial length (mm)	63	63	63	63
Air-gap length (mm)	0.3	0.3	0.3	0.3
Stator tooth arc (°)	5.18	5.18	15	15
Rotor tooth arc (°)	6.67	6.67	15	15
Permanent magnet width/ length — stator tooth (mm)	-	4.99/5.5	-	4.5/13
Number of turns per phase	80	80	80	80
Type of permanent magnet	-	Ndfeb35-SH	-	Ndfeb35-SH
Magnetic (electrical) steel material	M19-29G	M19-29G	M19-29G	M19-29G
Number of permanent magnets	-	3	-	6
Winding weight (kg)	1.424	1.424	1.424	1.424
Stator iron weight (kg)	2.37	2.37	1.952	1.952
Rotor iron weight (kg)	0.8847	0.8847	0.858	0.858
Permanent magnets weight (kg)	-	0.0136	-	0.191
Total effective motor weight (kg)	4.6787	4.6923	4.234	4.425

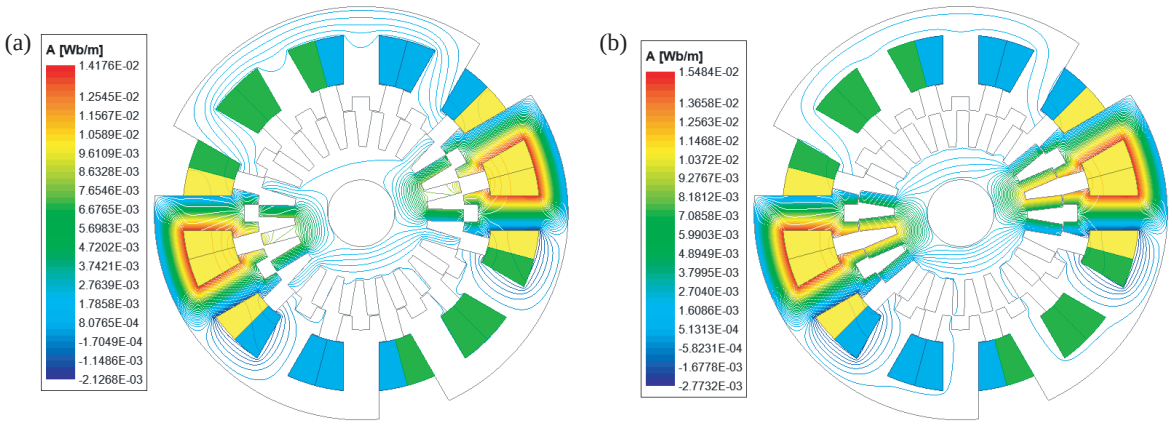

FIGURE 7. Flux lines at a current of 12 A: (a) unaligned position, (b) aligned position.

tively. The flux linkage increases with higher current and as the rotor approaches the aligned position.

- Figure 9(b) presents the variations in the motor's inductance under different currents. As the excitation current increases, inductance decreases due to magnetic core saturation and higher magnetic reluctance. At low currents, the core remains unsaturated, and inductance stays nearly constant, as the flux path reluctance is dominated by the air gap.

- Figure 9(c) depicts the flux linkage of the hybrid Switched Reluctance Motor with embedded magnets between the teeth versus rotor position, with 0° and 180° representing the unaligned and aligned positions. Similar to the conventional SRM, flux linkage increases with higher current and as the rotor moves toward the aligned position.

- Figure 9(d) shows the variations in inductance of the hybrid motor under different currents. Inductance decreases with increasing excitation due to core saturation and increased magnetic reluctance, while, at low currents, it remains nearly constant as the air gap primarily governs the flux path reluctance.

3.3. Static Torque Curves

Figure 10 illustrates the static torque curves, with the proposed motors defined as follows: S: Modular two-teeth Switched Re-

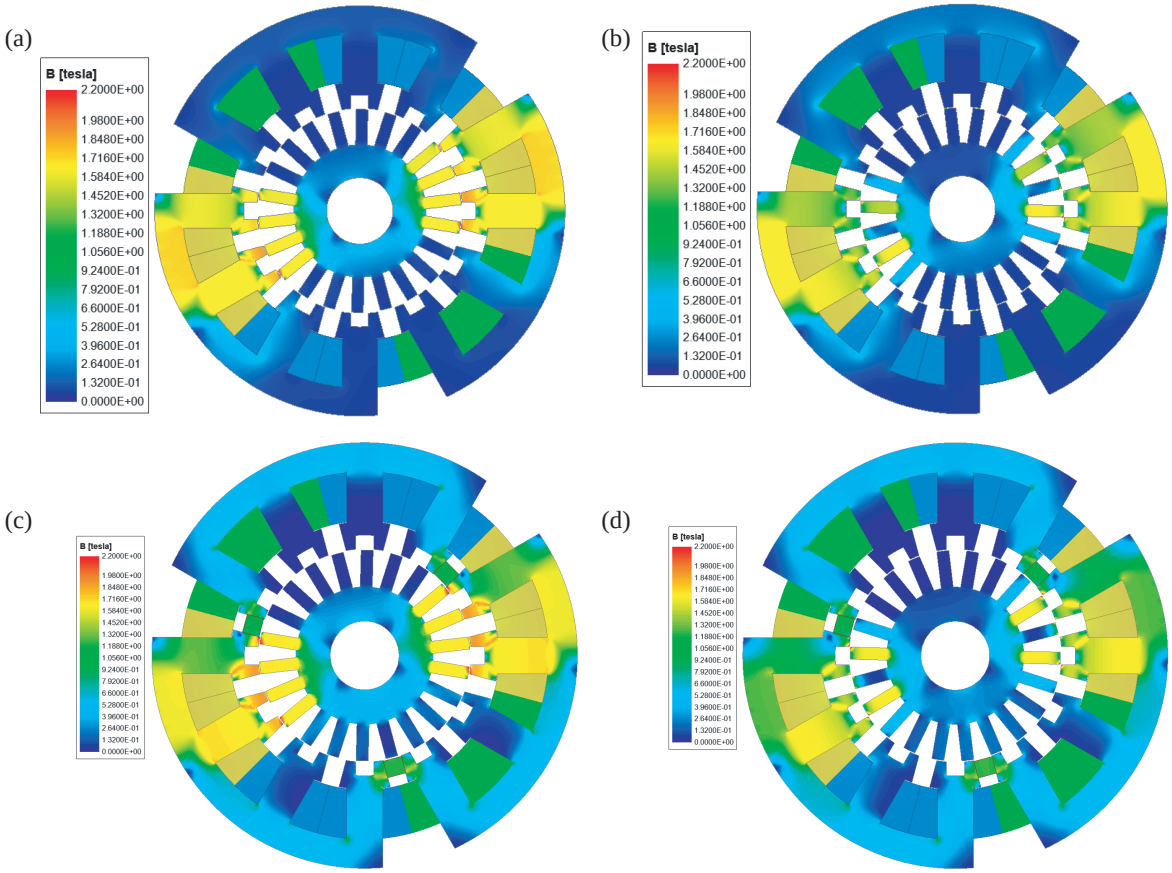

FIGURE 8. The magnetic flux density distribution in the aligned and unaligned positions. (a) and (b) the aligned and unaligned positions of the switched reluctance motor, respectively, (c) and (d) the aligned and unaligned positions of the hybrid switched reluctance motor with embedded magnets between the teeth.

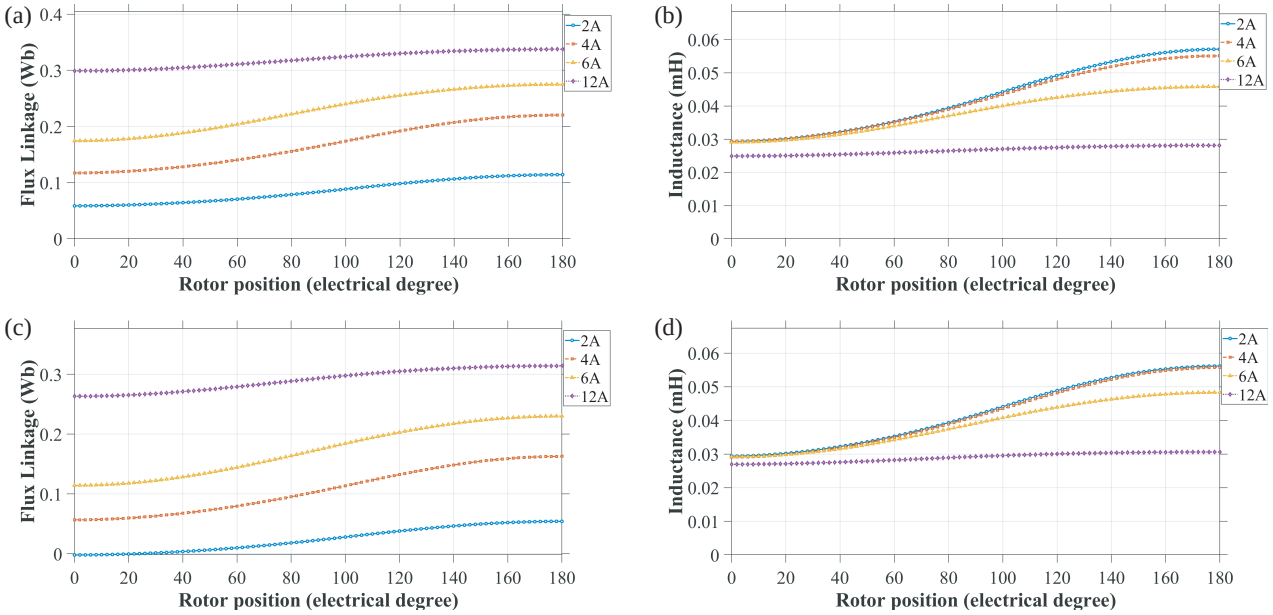

FIGURE 9. The flux linkage and inductance profiles of the proposed switched Reluctance Motor and the proposed hybrid Switched Reluctance Motor with embedded magnets between the teeth, as a function of rotor position and excitation currents of 2, 4, 6, and 12 A: (a) Flux linkage, (b) inductance of the proposed Switched Reluctance Motor, (c) flux linkage, and (d) inductance of the proposed hybrid Switched Reluctance Motor with embedded magnets between the teeth.

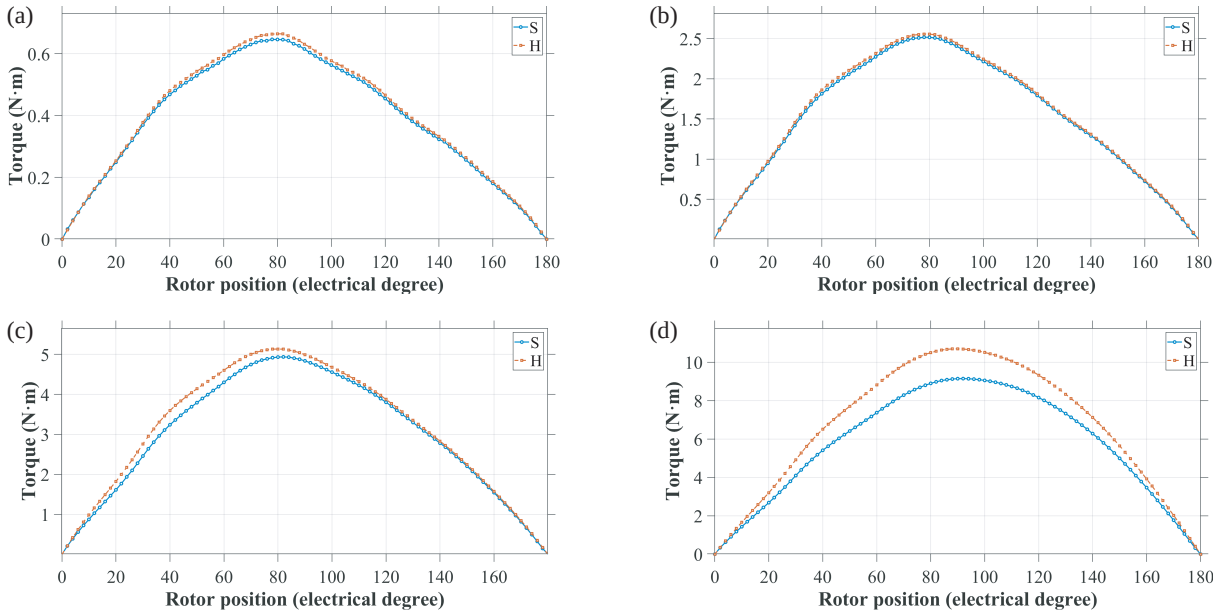

FIGURE 10. Static torque curves versus rotor position for the two proposed motors under different excitation currents: (a) 2 A, (b) 4 A, (c) 6 A, (d) 12 A.

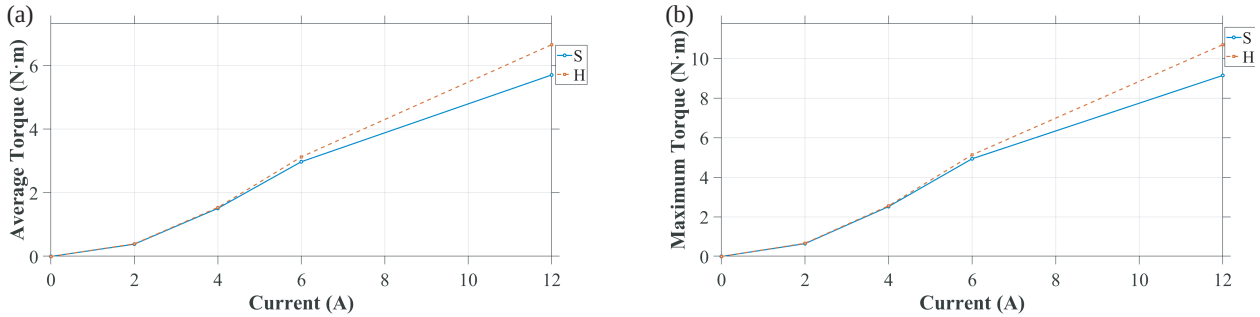

FIGURE 11. Static torque curves versus rotor position for the two proposed motors under different excitation currents: (a) average static torque, (b) maximum static torque.

luctance Motor; H: Hybrid Switched Reluctance Motor with inter-tooth permanent magnets.

Figures 10(a)–(d) present the torque profiles of these two motors under excitation currents of 2, 4, 6, and 12 A. The analysis indicates that the Hybrid Switched Reluctance Motor with inter-tooth permanent magnets produces substantially higher torque compared with the permanent-magnet-free model.

Furthermore, Figures 11(a) and 11(b) compare the average and maximum static torque values of the two motors at different excitation currents, confirming that the proposed hybrid motor achieves the highest average and peak torque.

3.4. Comparison with the Switched Reluctance Motor SRM12/10 and the Hybrid Switched Reluctance Motor HSRM12/10

To demonstrate the superiority of the proposed Hybrid Switched Reluctance Motor with inter-tooth permanent magnets, an HSRM12/10 and an SRM12/10 originally designed according to [28] and having dimensions similar to the proposed motor were redesigned and selected for comparison.

The torque performance of the proposed hybrid motor under different excitation currents is compared with that of the HSRM12/10 and SRM12/10 in Figure 12. The results show that the proposed motor delivers significantly higher torque than the other two motors.

Furthermore, Figure 13(a) presents the comparison of average torque, while Figure 13(b) shows the comparison of maximum torque for the three motors under various excitation currents.

For all excitation currents, the proposed Hybrid Switched Reluctance Motor with inter-tooth permanent magnets achieves both higher average and maximum torque compared to the HSRM12/10 and SRM12/10.

3.5. Investigation and Analysis of Cogging Torque

Figure 14 illustrates the cogging torque of the Hybrid Switched Reluctance Motor with inter-tooth permanent magnets. The torque magnitude is sufficiently low to be considered negligible. This is attributed to the fact that, when the windings are unexcited, only a small portion of magnetic flux passes through the rotor and the air gap.

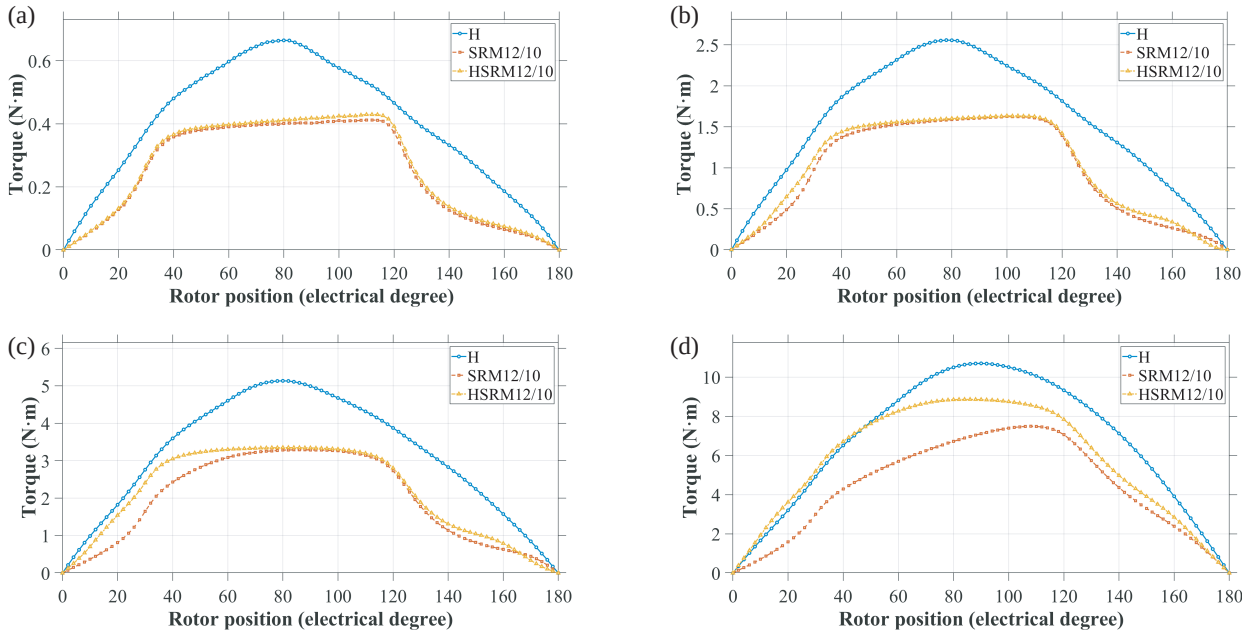

FIGURE 12. Static torque curves versus rotor position for the three motors under different excitation currents: (a) 2 A, (b) 4 A, (c) 6 A, (d) 12 A.

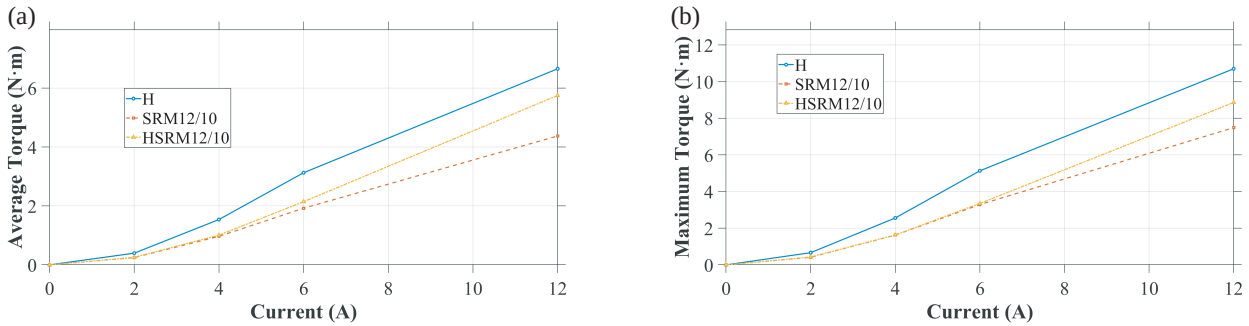

FIGURE 13. Comparison of the three motors' torque under different excitation currents: (a) average torque, (b) maximum torque.

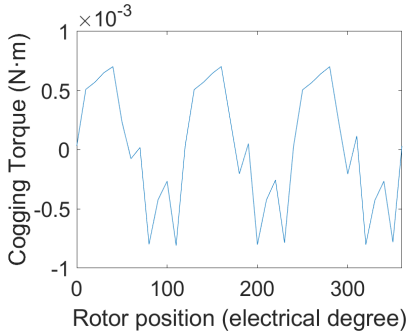

FIGURE 14. Cogging torque of the hybrid switched reluctance motor with inter-tooth permanent magnets.

3.6. Steady-State Performance

Figure 15 presents the simulation results of the proposed Switched Reluctance Motor at a low speed of 200 rpm. An asymmetrical three-phase converter with a 120° conduction angle was used in the simulation. The voltage, flux linkage, current, and torque waveforms were obtained using the Current-Controlled Chopping (CCC) method with a chopping current of 6 A and an input voltage of 170 V. The results show a root-mean-square (RMS) current of approximately 3.232 A and an average torque of about 3.2974 N · m.

Figure 16 illustrates the performance of the proposed motor at a high speed of 900 rpm. In this case, an asymmetrical three-phase converter with a 120° conduction pattern was employed, and the voltage, flux linkage, current, and torque waveforms were extracted using the Single-Pulse Control (SPC) method with an input voltage of 200 V. The results indicate an RMS current of approximately 2.99 A and an average torque of about 2.7948 N · m.

Figure 17 presents the simulation results of the proposed Hybrid Switched Reluctance Motor with inter-tooth permanent magnets at a low speed of 200 rpm. An asymmetrical three-phase converter with a 120° conduction angle was used in the simulation. The voltage, flux linkage, current, and torque waveforms were obtained using the CCC method with a chopping current of 6 A and an input voltage of 170 V. The results indicate an RMS current of approximately 3.23 A and an average torque of about 3.4634 N · m.

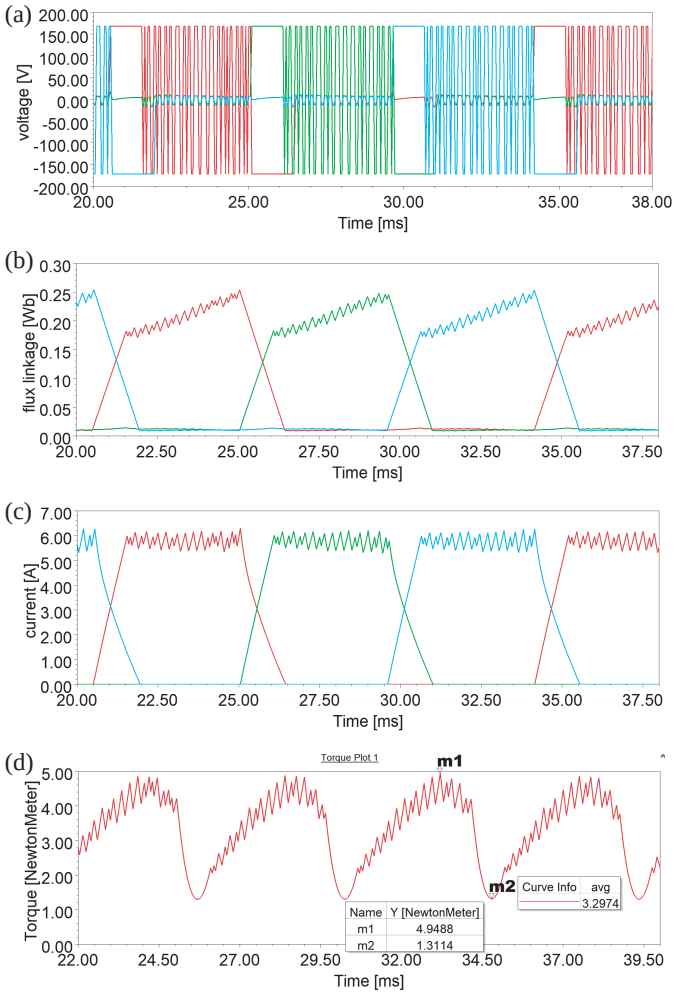

FIGURE 15. Steady-state performance of the proposed switched reluctance motor using the current chopping control (CCC) method.

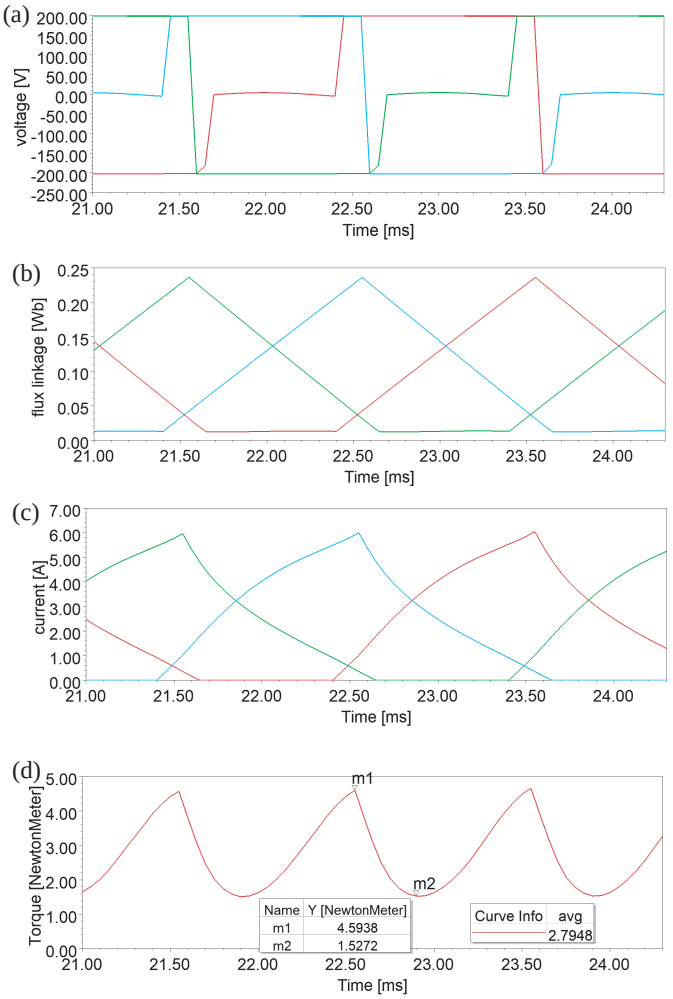

FIGURE 16. Steady-state performance of the proposed switched reluctance motor using the single-pulse control (SPC) method.

Figure 18 shows the performance of the proposed motor at a high speed of 900 rpm. In this case, an asymmetrical three-phase converter with a 120° conduction pattern was employed, and the voltage, flux linkage, current, and torque waveforms were extracted using the Single-Pulse Control (SPC) method with an input voltage of 200 V. The results indicate an RMS current of approximately 3.2 A and an average torque of about 3.0439 N · m.

3.6.1. Comprehensive Performance, Loss, and Efficiency Analysis

A rigorous characterization of losses and efficiency was conducted to provide a complete performance profile of the optimized HSSRM 24/22. The total power loss (P_{loss}) is analyzed in two main categories: copper losses (P_{cu}) and iron losses (P_{fe}). The iron losses, including hysteresis, eddy-current, and excess components, were extracted using the Transient FEA electromagnetic loss model in ANSYS Maxwell, while the copper losses were calculated based on the RI^2 method at the rated operating point.

The mechanical output power (P_{out}) and the overall energy efficiency (η) were derived based on the final optimized dimensions. As documented in the updated Table 4, the proposed design achieves an output power of 72.53 W and a total efficiency of 62.77%. Compared to the benchmark HSRM 12/10, which reports an efficiency of 56.95%, the proposed motor demonstrates a significant efficiency gain of 5.82%. This improvement, despite the higher magnetic loading, is a direct result of utilizing high-grade M19-29G steel and the optimized modular flux paths, which effectively manage the flux density distribution.

Furthermore, the symmetric magnetic flux density distribution presented in Figure 8 (based on the FEA results) indicates a balanced radial force density across the modular C-core segments. This symmetry is critical for mitigating electromagnetic vibration and acoustic noise. From a thermal perspective, the modularity of the stator provides an increased surface area for heat dissipation, ensuring that the motor operates reliably within safe thermal boundaries even at the increased torque density of 3.4634 N · m.

3.6.2. Dynamic Performance and Starting Characteristic Analysis

To validate the operational robustness of the proposed HSSRM 24/22, a series of transient dynamic simulations were performed. The analysis focuses on the machine's behavior during

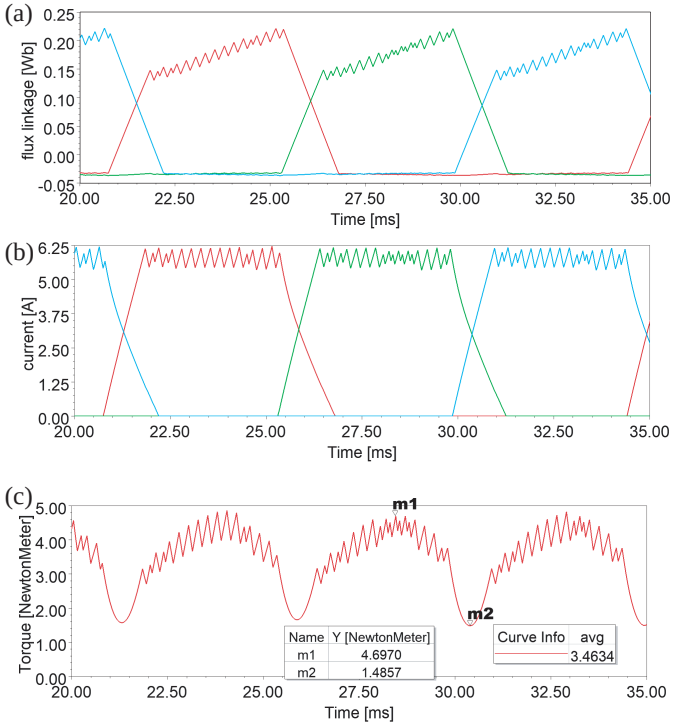

FIGURE 17. Steady-state performance of the proposed hybrid switched reluctance motor with inter-tooth permanent magnets using the current chopping control (CCC) method.

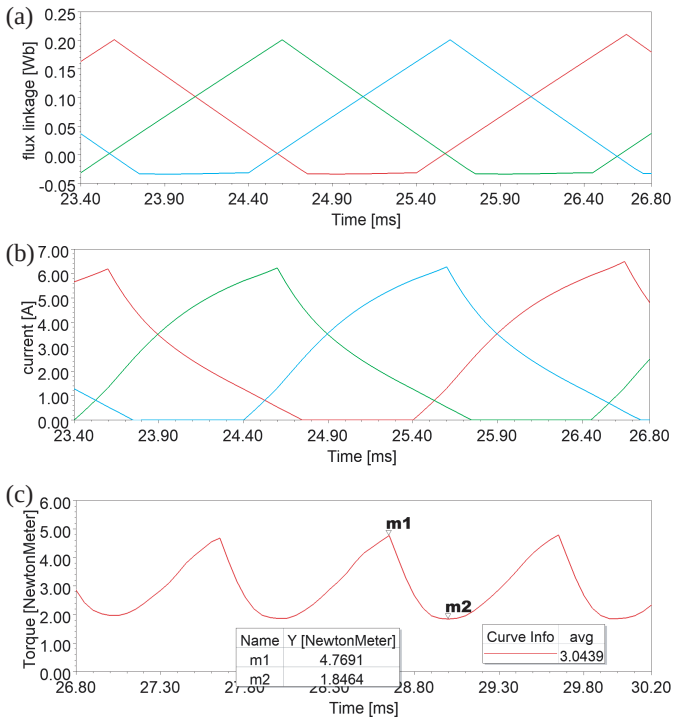

FIGURE 18. Steady-state performance of the proposed hybrid switched reluctance motor with inter-tooth permanent magnets using the single-pulse control (SPC) method.

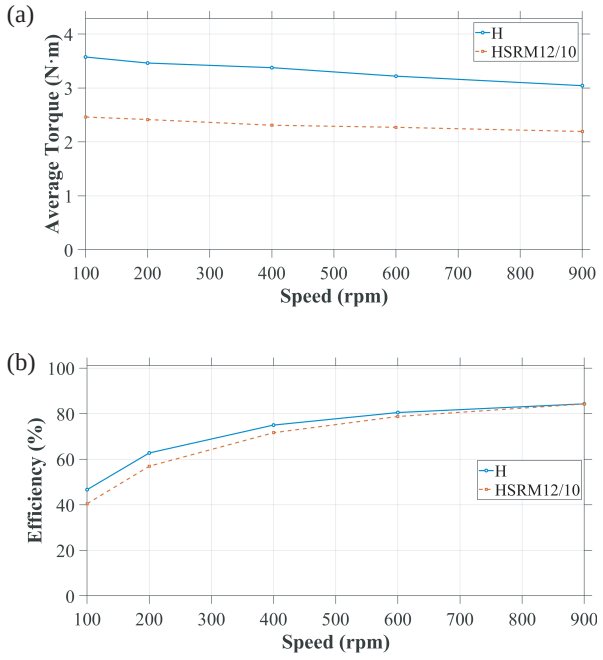

FIGURE 19. Comparative dynamic performance characteristics: (a) average torque versus speed for the proposed HSSRM 24/22 and the reference [28] HSRM, and (b) efficiency versus speed profiles, demonstrating the superior energy conversion capability of the proposed design.

the critical start-up phase and its performance across a variable speed range.

The starting performance was evaluated by applying a load inertia 25 times greater than the rotor inertia. The comparative

TABLE 3. Comparative overall performance metrics, loss distribution, and efficiency for the reference HSRM 12/10 [28] and the proposed optimized HSSRM 24/22.

Dynamic Parameter	HSRM12/10 [28]	H (Proposed)
Starting Torque [N · m] (at 3 ms)	2.98	2.35
Time to reach 200 RPM (ms)	54.4	36
Rise Time (ms)	48.7	27.9
Torque Ripple [%]	121.82	96.46
Max. Dynamic Torque [N · m]	3.373	4.8246

results between the proposed design and the HSRM 12/10 [28] are summarized in Table 3. It is observed that the proposed motor reaches 200 RPM in just 36 ms, whereas the reference motor requires 54.4 ms. Furthermore, the Rise Time of the 24/22 structure is 27.9 ms, marking a 42.7% improvement in dynamic responsiveness.

The transient waveforms for phase current, rotor speed, and electromagnetic torque during the starting period are illustrated in Figure 20. The proposed motor delivers a high starting torque of 2.35 N · m (at 3 ms), reaching a maximum dynamic torque of 4.824 N · m. Additionally, the torque ripple under dynamic loading is significantly lowered to 96.46%, compared to 121.8% for the reference design. These results, combined with the torque-speed and efficiency-speed characteristics (Fig-

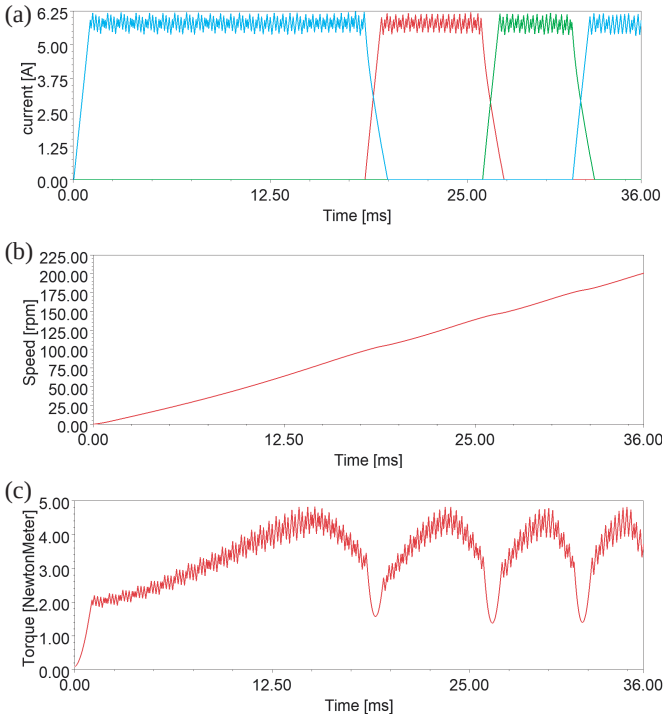

FIGURE 20. Transient starting performance of the proposed HSSRM 24/22 under a heavy inertia load (25x rotor inertia): (a) phase current waveforms showing the switching dynamics, (b) rotor speed response during the acceleration phase, and (c) dynamic torque profile showing the starting and peak torque capabilities.

ures 19(a) and (b)), confirm the proposed structural and transient performance of the machine.

Based on the data in Table 4, Motor H, which incorporates inter-tooth permanent magnets, exhibits outstanding performance in terms of average torque and output power. Compared with the SSRM24/22 motor of similar iron mass, this improvement is attributed to the proper placement and optimal utilization of the magnets, which enhance both torque and power density.

Moreover, compared with the reference motors [28], namely the SRM12/10 and HSRM12/10 of similar dimensions, both proposed motors deliver higher average torque and power, while also achieving a superior power-to-iron-mass ratio. These results clearly indicate that the proposed designs offer higher efficiency than the reference models [28].

3.7. Magnetic Saturation and Material Characterization

The electromagnetic performance of the proposed HSSRM 24/22 is deeply linked to the nonlinear magnetic properties of the M19-29G electrical steel. As shown in the provided B-H curve, the material transitions into the saturation region beyond 1.8 T.

Under rated excitation, the flux density distribution (Figure 21) reveals that the stator teeth reach a peak density of 2.0 T to 2.2 T. This deep saturation in the modular teeth is a deliberate design choice to maximize the torque density. However, the modular C-core structure effectively manages the flux path, ensuring that the stator yoke remains at a lower magnetic loading of approximately 1.4 T, which is below the deep saturation knee. This strategic flux distribution allows for high torque production while simultaneously controlling core losses in the back iron, balancing power density with overall efficiency.

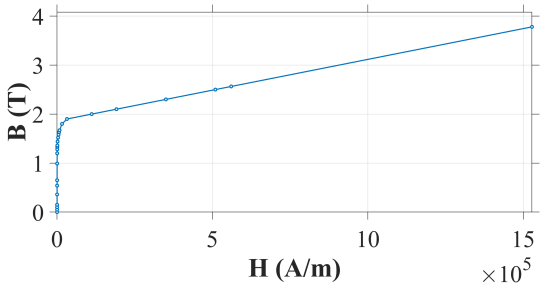

FIGURE 21. B-H curve of M19-29G material.

3.8. Demagnetization Safety and PM Stability Analysis

The stability of the integrated NdFe35_SH permanent magnets is a critical factor for the reliability of the hybrid excitation. The magnet material is characterized by a high coercive force ($H_c = -1,500,000$ A/m).

To evaluate the demagnetization risk, the flux density within the magnets was examined under peak-load conditions. As illustrated in the demagnetization analysis (Figure 22), the minimum flux density within the magnet volume remains significantly above the irreversible demagnetization threshold. Even during high-current transients at 6 A, the operating points stay within the linear region of the magnet's B-H curve. This confirms a robust safety margin, ensuring that the motor maintains its performance without any irreversible loss of magnetization over its operational life.

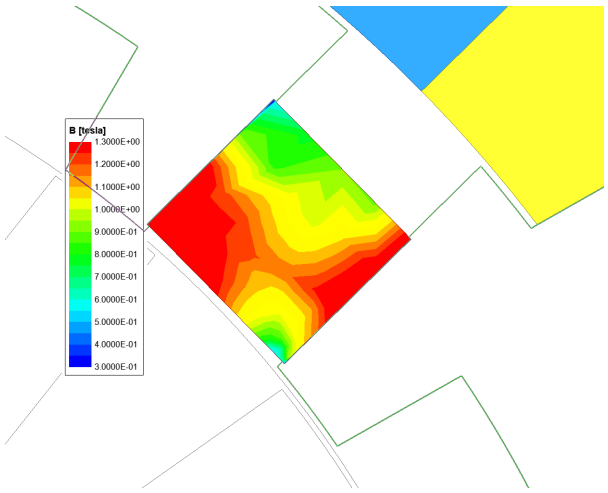

FIGURE 22. Flux density distribution in the NdFe35_SH magnet.

3.9. Cost-Benefit Analysis and PM Impact

A critical observation in the proposed design is the high impact of a very small amount of permanent magnet material. According to the design specifications, the total magnet mass is only 0.0136 kg. Despite this minimal usage, the comparative analysis shows a substantial performance boost:

TABLE 4. Comparison of the performance of the two proposed motors and the two reference motors [28] at different speeds.

	SSRM24/22 (Proposed)		H (Proposed)		SRM12/10 [28]		HSRM12/10 [28]	
Control Mode	CCC	SPC	CCC	SPC	CCC	SPC	CCC	SPC
Speed (rpm)	200	900	200	900	200	900	200	900
DC Link Voltage (V)	170	200	170	200	170	200	170	200
Phase RMS Current (A)	3.232	2.99	3.23	3.2	3.08	2.58	3.08	2.88
Average Torque [N · m]	3.2974	2.7948	3.4634	3.04	2.16	1.58	2.41	2.19
Torque per Ampere [N · m/A]	1.02	0.93	1.07	0.95	0.7	0.61	0.78	0.76
Torque per Iron Mass [N · m/kg]	0.704	0.597	0.738	0.647	0.51	0.37	0.54	0.49
Torque Ripple [%]	107.67	109.72	92.7	96	109.6	125	122	124
Output Power (W)	69.06	263.4	72.53	286.8	45.25	148	50.5	206.7
Output Power per Ampere [W/A]	21.36	88.09	22.45	89.62	14.6	57.3	16.3	71.77
Power per Iron Mass [W/kg]	14.76	56.29	15.45	61.12	10.68	34.9	11.3	46.7
Core Loss [w]	5.166	15.6346	5.466	16.5	4.04	8.86	3.96	8.73
Copper loss [w]	37.604	32.184	37.55	36.8	34.28	23.9	34.28	29.85
Efficiency [%]	61.75	84.63	62.77	84.31	54.14	81.9	56.9	84.2

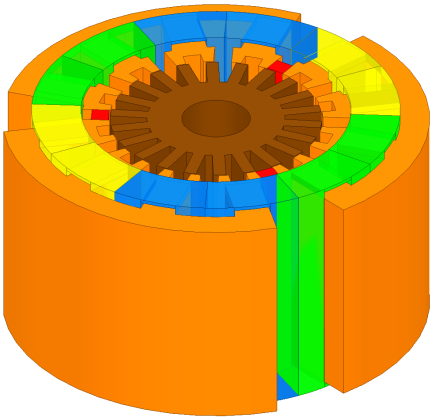

FIGURE 23. Flux density distribution in the NdFe35_SH magnet.

- Average Torque (Without PMs): 3.2974 N · m
- Average Torque (With PMs): 3.4634 N · m

This result represents an increase of approximately 5.03% in average torque using only a negligible amount of PM material. The reason for this significant improvement with such a low mass lies in the flux-focusing effect of the dual-tooth modular topology. In this structure, the magnets do not act as the sole source of MMF, but rather as magnetic valves. They effectively block the leakage flux in the stator slots and redirect it into the main air gap. By converting what would otherwise be wasted leakage flux into torque-producing flux, the proposed HSSRM 24/22 achieves an exceptional torque-per-magnet-mass ratio, making it a highly cost-effective solution for industrial drives.

3.10. 3D FEA Validation and End-Effect Analysis

To provide a comprehensive validation of the electromagnetic design and to account for axial flux leakage and end-winding effects often neglected in simplified models, a full-scale three-dimensional Finite Element Analysis (3D FEA) was performed.

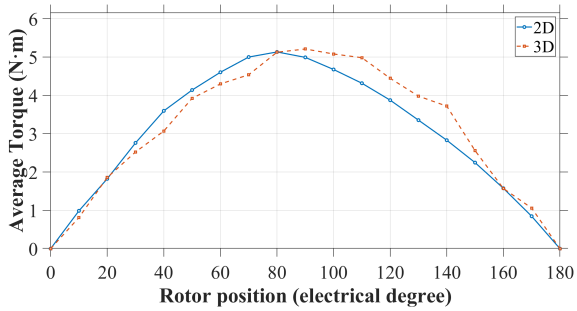

FIGURE 24. Comparative diagram of static torque profile in 2D and 3D analyses.

The 3D geometry of the proposed hybrid modular switched reluctance motor, as illustrated in Figure 23, precisely models the axial depth of the C-core segments and the permanent magnets.

The comparative analysis between the 2D and 3D FEA results for the static torque profile is presented in Figure 24. At a constant excitation current of 6 A, the following results were obtained:

- Average Torque (2D FEA): 2.98 N · m
- Average Torque (3D FEA): 3.08 N · m

The 3D FEA results show an excellent correlation with the 2D model, with a minor discrepancy of approximately 3.3%. Interestingly, the average torque calculated in the 3D environment is slightly higher than the 2D prediction. This phenomenon indicates that in the proposed modular dual-tooth topology, the fringing effects at the ends of the stator and rotor stacks contribute positively to the total flux linkage rather than acting as a traditional loss mechanism.

Furthermore, the 3D analysis confirms that the modular C-core structure effectively contains the magnetic field within the active stack length, minimizing the impact of end leakage on the air-gap flux density. This validation proves that the 2D FEA results used for the initial optimization are reliable and that the

actual prototype is expected to deliver slightly superior performance due to these beneficial three-dimensional magnetic field distributions.

4. CONCLUSION

In this study, a high-torque 24/22 modular C-core hybrid-excited switched reluctance motor (HESRM) was proposed, optimized, and analyzed. The core novelty includes the targeted integration of permanent magnets (PMs) within the inter-tooth spaces, which effectively reshapes the magnetic circuit and overcomes the torque density limitations of conventional SRMs. By employing a Multi-Objective Genetic Algorithm (GA) for structural refinement and a Magnetic Equivalent Circuit (MEC) for analytical verification, the design demonstrates high scientific soundness. A critical contribution of this work is the Three-Dimensional Finite Element Analysis (3D FEA) validation, which accounted for end-leakage effects and yielded an average torque of $3\,\mathrm{N}\cdot\mathrm{m}$, showing excellent agreement with the 2D FEA result of $2.98\,\mathrm{N}\cdot\mathrm{m}$. The performance results indicate that the HSSRM 24/22 achieves a 43% increase in average torque and superior efficiency compared to the benchmark HSRM 12/10 reported in the literature. Detailed evaluations of copper and iron losses, along with dynamic torque-speed and efficiency maps, confirm that the proposed topology maintains high performance across its entire operating range with a superior torque-per-PM-volume ratio. Ultimately, this research presents a robust, energy-efficient, and cost-effective motor design suitable for advanced high-torque electric drive systems.

REFERENCES

[1] Mecrow, B. C., E. A. El-Kharashi, J. W. Finch, and A. G. Jack, "Preliminary performance evaluation of switched reluctance motors with segmental rotors," *IEEE Transactions on Energy Conversion*, Vol. 19, No. 4, 679–686, Dec. 2004.

[2] Ullah, S., S. P. McDonald, R. Martin, M. Benarous, and G. J. Atkinson, "A permanent magnet assist, segmented rotor, switched reluctance drive for fault tolerant aerospace applications," *IEEE Transactions on Industry Applications*, Vol. 55, No. 1, 298–305, Jan.–Feb. 2019.

[3] Szabo, L. and M. Ruba, "Segmental stator switched reluctance machine for safety-critical applications," *IEEE Transactions on Industry Applications*, Vol. 48, No. 6, 2223–2229, Nov.–Dec. 2012.

[4] Davarpanah, G., J. Faiz, and H. Shirzad, "A C-core connected two-phase switched reluctance motor with embedded permanent magnets for developed torque enhancement," *IEEE Transactions on Industrial Electronics*, Vol. 71, No. 3, 2332–2342, Mar. 2024.

[5] Mao, S.-H. and M.-C. Tsai, "A novel switched reluctance motor with C-core stators," *IEEE Transactions on Magnetics*, Vol. 41, No. 12, 4413–4420, Dec. 2005.

[6] Masoumi, M. and M. Mirsalim, "E-core hybrid reluctance motor with permanent magnets inside stator common poles," *IEEE Transactions on Energy Conversion*, Vol. 33, No. 2, 826–833, Jun. 2018.

[7] Madhavan, R. and B. G. Fernandes, "Axial flux segmented SRM with a higher number of rotor segments for electric vehicles," *IEEE Transactions on Energy Conversion*, Vol. 28, No. 1, 203–213, Mar. 2013.

[8] Wang, G., H. Chen, F. Yu, W. Yan, X. Wang, M. Benbouzid, A. de A. Bresolin, M. P. Aguirre, H. Torkaman, M. Shamiev, Y. Tairov, M. Orabi, and M. A. Gaafar, "Design, analysis, and comparison of a novel axial flux modular-double-stator hybrid excitation SRM," *IEEE Transactions on Transportation Electrification*, Vol. 10, No. 3, 6100–6114, Sep. 2024.

[9] Lu, K., P. O. Rasmussen, S. J. Watkins, and F. Blaabjerg, "A new low-cost hybrid switched reluctance motor for adjustable-speed pump applications," *IEEE Transactions on Industry Applications*, Vol. 47, No. 1, 314–321, Jan.–Feb. 2011.

[10] Lu, K., U. Jakobsen, and P. O. Rasmussen, "Single-phase hybrid switched reluctance motor for low-power low-cost applications," *IEEE Transactions on Magnetics*, Vol. 47, No. 10, 3288–3291, Oct. 2011.

[11] Xu, L., D. Xu, X. Zhu, C. Zhang, and X. Zang, "Multimode excitation analysis and design of a new hybrid excited modular stator permanent magnet switched reluctance machine," *IEEE Transactions on Magnetics*, Vol. 59, No. 11, 1–6, Nov. 2023.

[12] Hasegawa, Y., K. Nakamura, and O. Ichinokura, "A novel switched reluctance motor with the auxiliary windings and permanent magnets," *IEEE Transactions on Magnetics*, Vol. 48, No. 11, 3855–3858, Nov. 2012.

[13] Wang, F., B. Kou, L. Zhang, and C. Huang, "Analysis and optimal design of hybrid magnetic circuit reluctance direct drive motor," *IEEE Access*, Vol. 13, 26 420–26 428, 2025.

[14] Zhu, J., K. W. E. Cheng, and X. Xue, "Design and analysis of a new enhanced torque hybrid switched reluctance motor," *IEEE Transactions on Energy Conversion*, Vol. 33, No. 4, 1965–1977, Dec. 2018.

[15] Kondelaji, M. A. J., E. F. Farahani, and M. Mirsalim, "Teethed-pole switched reluctance motors assisted with permanent magnets: Analysis and evaluation," *IEEE Transactions on Energy Conversion*, Vol. 36, No. 3, 2131–2140, Sep. 2021.

[16] Du, Y., C. Zhang, X. Zhu, F. Xiao, Y. Sun, Y. Zuo, and L. Quan, "Principle and analysis of doubly salient PM motor with Π-shaped stator iron core segments," *IEEE Transactions on Industrial Electronics*, Vol. 66, No. 3, 1962–1972, Mar. 2019.

[17] Kondelaji, M. A. J., E. F. Farahani, and M. Mirsalim, "Performance analysis of a new switched reluctance motor with two sets of embedded permanent magnets," *IEEE Transactions on Energy Conversion*, Vol. 35, No. 2, 818–827, Jun. 2020.

[18] Tai, W.-H., M.-C. Tsai, Z.-L. Gaing, P.-W. Huang, and Y.-S. Hsu, "Novel stator design of double salient permanent magnet motor," *IEEE Transactions on Magnetics*, Vol. 50, No. 4, 1–4, Apr. 2014.

[19] Hwang, H., S. Bae, and C. Lee, "Analysis and design of a hybrid rare-earth-free permanent magnet reluctance machine by frozen permeability method," *IEEE Transactions on Magnetics*, Vol. 52, No. 7, 1–4, Jul. 2016.

[20] Wang, H., Y. Xue, J. Du, and H. Li, "Design and evaluation of modular stator hybrid-excitation switched reluctance motor for torque performance improvement," *IEEE Transactions on Industrial Electronics*, Vol. 71, No. 10, 12 814–12 823, Oct. 2024.

[21] Amirkhani, M., M. A. J. Kondelaji, A. Ghaffarpour, M. Mirsalim, and S. Vaez-Zadeh, "Study of boosted toothed biased flux permanent magnet motors," *IEEE Transactions on Transportation Electrification*, Vol. 8, No. 2, 2549–2564, Jun. 2022.

[22] Davarpanah, G., J. Faiz, H. Shirzad, and M. Lotfizadeh, "A modular hybrid excited switched reluctance motor with two groups of permanent magnets to enhance the performance of the motor," *IEEE Transactions on Energy Conversion*, Vol. 39, No. 3, 1686–1698, Sep. 2024.

[23] Zhu, J., K. W. E. Cheng, X. Xue, and Y. Zou, "Design of a new enhanced torque in-wheel switched reluctance motor with

divided teeth for electric vehicles," *IEEE Transactions on Magnetics*, Vol. 53, No. 11, 1–4, Nov. 2017.

[24] Farahani, E. F., M. A. J. Kondelaji, and M. Mirsalim, "A new exterior-rotor multiple teeth switched reluctance motor with embedded permanent magnets for torque enhancement," *IEEE Transactions on Magnetics*, Vol. 56, No. 2, 1–5, Feb. 2020.

[25] Farahani, E. F., M. A. J. Kondelaji, and M. Mirsalim, "A new exterior-rotor multiple teeth switched reluctance motor with embedded permanent magnets for torque enhancement," *IEEE Transactions on Magnetics*, Vol. 56, No. 2, 1–5, Feb. 2020.

[26] Li, G. J., Z. Q. Zhu, M. Foster, and D. Stone, "Comparative studies of modular and unequal tooth PM machines either with or without tooth tips," *IEEE Transactions on Magnetics*, Vol. 50, No. 7, 1–10, Jul. 2014.

[27] Ding, W., S. Yang, Y. Hu, S. Li, T. Wang, and Z. Yin, "Design consideration and evaluation of a 12/8 high-torque modular-stator hybrid excitation switched reluctance machine for EV applications," *IEEE Transactions on Industrial Electronics*, Vol. 64, No. 12, 9221–9232, Dec. 2017.

[28] Ding, W., H. Fu, and Y. Hu, "Characteristics assessment and comparative study of a segmented-stator permanent-magnet hybrid-excitation SRM drive with high-torque capability," *IEEE Transactions on Power Electronics*, Vol. 33, No. 1, 482–500, Jan. 2018.

[29] Ding, W., S. Yang, and Y. Hu, "Development and investigation on segmented-stator hybrid-excitation switched reluctance machines with different rotor pole numbers," *IEEE Transactions on Industrial Electronics*, Vol. 65, No. 5, 3784–3794, May 2018.

[30] Ding, W., H. Bian, K. Song, Y. Li, and K. Li, "Enhancement of a 12/4 hybrid-excitation switched reluctance machine with both segmented-stator and-rotor," *IEEE Transactions on Industrial Electronics*, Vol. 68, No. 10, 9229–9241, Oct. 2021.

[31] Farahani, E. F., M. A. J. Kondelaji, and M. Mirsalim, "An innovative hybrid-excited multi-tooth switched reluctance motor for torque enhancement," *IEEE Transactions on Industrial Electronics*, Vol. 68, No. 2, 982–992, Feb. 2021.